THE JOURNAL OF PHYSICAL CHEMISTRY C
A JOURNAL OF THE AMERICAN CHEMICAL SOCIETY

pubs.acs.org/JPCC

Article

Van der Waals Stacked 2D-Layered $Co_2Ge_2Te_6$ with High Curie Temperature and Large Magnetic Crystal Anisotropy

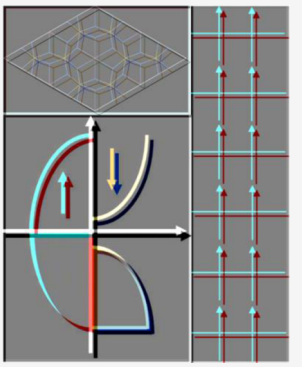
Zhaoyong Guan,* Linhui Lv, Ziyuan An, Ya Su, Yanyan Jiang, Xuming Wu, and Shuang Ni*

Cite This: *J. Phys. Chem. C* 2023, 127, 5991−6001

Read Online

ACCESS | Metrics & More | Article Recommendations | Supporting Information

ABSTRACT: $Co_2Ge_2Te_6$ shows an intrinsic ferromagnetic order, which originates from the superexchange interaction between Co and Te atoms, with a Curie temperature of 161 K. The $Co_2Ge_2Te_6$ monolayer is half-metal, and the spin-β electron is a semiconductor with a gap of 1.311 eV. The $Co_2Ge_2Te_6$ monolayer shows in-plane anisotropy, with a magnetic anisotropy energy (MAE) of −10.2 meV/f.u., and Te atoms contribute −9.94 meV/f.u. Moreover, the bilayer with AA- and AB-stackings has MAEs of −24.659 and −24.492 meV/.f.u., respectively. Most interestingly, bilayers present ferromagnetic half-metallicity independent of stacking orders. The multilayers ($N \geq 6$) present ferromagnetic half metal, while magnetoelectronic properties are related with stacking patterns in thinner multilayers. Moreover, the magnetoelectronic properties of bulk are related with stacking patterns. The multilayers' magnetic orders are determined by the super−super exchange and weak van der Waals (vdW) interaction. Moreover, the $Co_2Ge_2Te_6$ monolayer and multilayers show good dynamical and thermal stability. These findings could pave the way of application of intrinsic ferromagnetic $Co_2Ge_2Te_6$ in the spintronics.



Downloaded via SHANDONG UNIV on April 3, 2023 at 02:37:33 (UTC).
See https://pubs.acs.org/sharingguidelines for options on how to legitimately share published articles.

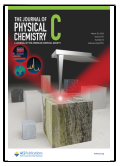
1. INTRODUCTION

Two-dimensional (2D) intrinsic ferromagnetic materials, especially half-metal (HM), are urgent for the spintronics.[1,2] All kinds of 2D materials, such as graphene,[3] h-BN,[4] MoS_2,[5,6] and stanene,[7] have been successfully synthesized in the recent years. However, 2D magnetic materials, especially ferromagnetic materials, are rare.[8,9] It is limited by the Mermin−Wagner theory,[10] which implies 2D magnetic materials cannot exist in the isotropic Heisenberg model at finite temperature. However, CrI_3,[11] VSe_2,[12] $FeGeTe_2$,[13,14] $CrGeTe_3$ (CGT) monolayer (ML),[15−17] and self-intercalation of 2D layered materials[18,19] with intrinsic ferromagnetism have been successfully synthesized in the experiments. 2D magnetic materials have a wide application in the condensed physics and spintronics.[20] Therefore, 2D magnetic materials are becoming a hot topic in research.[1,21] Ideal 2D magnetic materials are expected to have attractive properties,[2,22−24] such as high Curie temperature (T_c), MAE with an easy magnetization axis (EA) along out of the plain,[25] and high spin polarization. For magnetic materials, half-metallic materials are amazing, whose one spin channel is insulative or semiconductive, while another channel is conductive.[26] As a result, HM could get 100% spin-polarized current, which are highly desired in the spintronics. The perfect HM used in the spintronics is expected a higher T_c, and the semiconductive gap should be large enough.[2] Furthermore, a large MAE is urgently needed to retain half-metallicity at high temperature in the electronics.[27,28]

2D ferromagnetic HMs are rare. Graphene nanoribbon (GNR) could be transformed into HM with an external electric field.[29] The chemically functioned GNR could be also transformed into HM.[30] Furthermore, carrier[25] and defect[31] could effectively convert semiconductors into HM, but these strategies are hard to achieve in the experiments.[32,33] Among 2D magnetic materials, only CrI_3,[11,34] VSe_2 (T phase),[12] and CGT[15] are ferromagnetic semiconductors, while Fe_3GeTe_2[14,35] and $CrSe_2$[36] are spin-polarized metal with a ferromagnetic (FM) order. Moreover, electronic properties of VSe_2 are dependent on the substrate.[12] In a word, the intrinsic HM is rare in 2D materials.[22] However, 2D HM is highly expected in the spintronics.[32,33] Moreover, the magnetoelectric properties of 2D materials are related with d electrons' configuration. The CGT is a semiconductor. What are the properties of $M_2Ge_2Te_6$, as the Cr atom in CGT is replaced with other metals? In this work, we have constructed and found half-metallic $Co_2Ge_2Te_6$ ML and multilayers with intrinsic ferromagnetism by a global minimum search and density functional theory (DFT).

In this paper, the electronic and magnetic properties of $Co_2Ge_2Te_6$ are systematically investigated by DFT. $Co_2Ge_2Te_6$ ML is an intrinsic ferromagnetic material, which originates from the superexchange interaction between Co and Te atoms. $Co_2Ge_2Te_6$ ML has a T_c of 161 K. The intrinsic ferromagnetism could be concluded by the Goodenough−Kanamori−Anderson (GKA) theory.[37−39] $Co_2Ge_2Te_6$ ML is a

Received: December 9, 2022
Revised: February 13, 2023
Published: March 17, 2023



ACS Publications

© 2023 American Chemical Society

HM with a band gap of 1.311 eV for spin-β electron, while the spin-α electron is conducting. $Co_2Ge_2Te_6$ ML and bilayer intend in-plane anisotropy (IPA), with MAEs of −10.2, −24.659 (AA), and −24.492 (AB) meV/f.u., respectively. Besides that, $Co_2Ge_2Te_6$ bilayers retain HM with the FM order, independent of stacking orders. For multilayers ($N \geq 6$), the layers prefer to ferromagnetically couple with each other, and they are all HM. However, the magnetoelectric properties of bulk are related with stacking patterns. Bulk of AA-stacking shows an AFM order, while AB-stacking shows the FM order, and both of them are normal spin-polarized metal. Our research implies robust ferromagnetic half-metallic $Co_2Ge_2Te_6$ with high T_c, large MAE, making it wide potential application in the magnetics and spintronics.

2. COMPUTATIONAL DETAILS

The calculation of $Co_2Ge_2Te_6$ is using plane-wave basis Vienna Ab initio Simulation Package (VASP) code[40] based on DFT. The Perdew−Burke−Ernzerhof (PBE)[41] is adopted to deal with 3d electrons' interaction. Moreover, Co's 3d electron is dealt with the art of hybrid-functional HSE06[42,43] and LDA + U method,[44] respectively. The energies of different orders, band structures, density of states (DOS), and magnetic exchange parameters are calculated by the art of HSE06 functional. Moreover, MAE, phonon spectra, and molecular dynamics are calculated by the LDA + U method.[44] The effective onsite Coulomb interaction parameter (U) and exchange interaction parameter (J) are set to be 7.70 and 0.70 eV, respectively. The effective U_{eff} ($U_{eff} = U - J$) is 7.00 eV,[45,46] and the corresponding energies of magnetic order and electronic properties are consistent with the HSE06 functional. The vacuum space in the z-direction is set 16 Å. The kinetic energy cutoff is set as 300 eV, and geometries are fully relaxed until energy and force are converged to 10^{-6} eV and 1 meV/Å, respectively. 6 × 6 × 1 and 9 × 9 × 1 Monkhorst−Pack grids[47] are used for the geometry optimization and energy calculation, respectively. The magnetocrystalline anisotropy (MCA) energy is calculated with an energy cutoff of 400 eV, and the energy is less than 1×10^{-8} eV. The spin−orbital coupling (SOC) effect is also taken into account for determining magnetic anisotropy. The corresponding adopted k-grid is 19 × 19 × 1, after a systematical test, as shown in Figure S1. The phonon spectra and DOS are calculated using the finite displacement method as implemented in the phonopy package.[48] A 4 × 4 × 1 cell is adopted, and total energy and Hellmann−Feynman force are converged to 10^{-8} eV and 1 meV/Å in the phonon spectra calculation, respectively. 1000 uniform k-points along high-symmetry lines are used to obtain phonon spectra. In order to confirm dynamical stability, ab initio molecular dynamics (AIMD) simulation is also performed. The constant moles−volume−temperature (NVT) ensemble with Nosé−Hoover thermostat[49] is adopted at temperatures of 300 and 500 K, respectively. The time step and total time are 1 fs and 10 ps, respectively. A larger supercell (2 × 2 × 1 cell) is adopted in the AIMD simulation to eliminate effect of the periodic boundary condition with a smaller system size. In order to describe the vdW interaction, the DFT-D2 method[50] is used. The calculated distance between graphene layers is 3.25 Å,[51] which is consistent with the experiment.

3. RESULTS AND DISCUSSION

3.1. Geometry of $Co_2Ge_2Te_6$ ML. The geometry of $Co_2Ge_2Te_6$ ML is fabricated and confirmed by particle swarm optimization (PSO)[52] and AISP based on the crystal structure analysis, shown in Figure 1a−c. The corresponding optimized

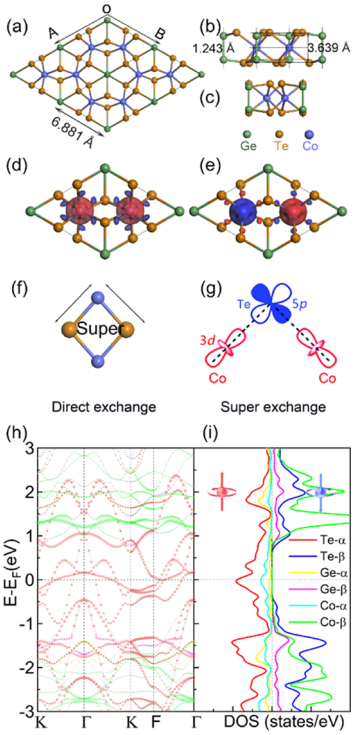


Figure 1. (a) Top, (b) side-1 (along x axis), and (c) side-2 (along y axis) views of optimized geometries of $Co_2Ge_2Te_6$ ML. The green, yellow, and blue balls represent Ge, Te, and Co atoms. (d,e) Spin charge density difference of (c) FM and (d) AFM orders. The isovalue is 0.02 e/Å^3. (f) Direct exchange and (g) superexchange interaction. (h) Atom projected band structures. (i) PDOS with FM order. The red, blue, yellow, pink, cyan, and green lines represent projected band structure and PDOS of Te-α, Te-β, Ge-α, Ge-β, and Co-α and Co-β atoms, respectively. The Fermi-level is set to 0 eV.

lattice parameter is $a = b = 6.881$ Å, by fitting energy with lattice parameters, which is larger than 6.810 Å of CGT.[53] It shows that Co atom's ionic radius (65) is larger than the Cr atom (62). The bond length between Co and Te atoms is 2.836 Å, while the bond length between Ge and Te atoms is 2.618 Å. The bond length between Ge and Ge atoms is 2.485 Å. $Co_2Ge_2Te_6$ ML shows a D_{3d} point group, which is the same with CGT. The vertical distance between Te and Te atoms is 3.639 Å, shown in Figure 1b.

The Co atom is in the center of the octahedron, similar to the Cr atom in CGT. There is 1.011 e electron transfer from Co atoms to Ge (0.396 e), and Te (0.691 e) atoms by Bader analysis.[54] The Co atom shows a $3d^84s^1$ configuration, resulting in Co^{1+} ions, as one d electron is taken away. The Co atom has a high-spin octahedral d^8 configuration, leading to a magnetic moment (MM) of 2.04 μ_B, while Ge atoms have −0.01 (0.01 × 2) μ_B. There are six Te atoms, which have −0.06 (×2), −0.05 (×2), and −0.02 (×2) μ_B MM, respectively. Each supercell has two Co atoms. Therefore, there are two kinds of orders, including FM and antiferromagnetic (AFM) orders, and the corresponding spin charge density difference is shown in Figure 1d,e, respectively.

https://doi.org/10.1021/acs.jpcc.2c08648
J. Phys. Chem. C 2023, 127, 5991−6001

MM mainly localizes in Co atoms, shown in Figure 1d,e, which is consistent with above analysis. The total MM is 4.00 μ_B for FM order, while the total MM is 0.00 μ_B for the AFM order. In order to describe magnetic stability, we define energy difference (ΔE) between FM and AFM orders: $\Delta E = E_{AFM} - E_{FM}$. Moreover, the corresponding ΔE is 0.11 eV, which implies that $Co_2Ge_2Te_6$ ML shows the FM ground state.

In this section, the reason for $Co_2Ge_2Te_6$ ML showing a FM order is investigated. Each Co atom is coordinated by six ligands-Te in $Co_2Ge_2Te_6$ ML, and the corresponding Te−Co−Te bond angles are 91.07, 83.27, and 103.20°, respectively. According to Goodenough−Kanamori−Anderson rules[37−39] of superexchange theorem, it results in FM coupling (shown in Figure 1f,g). However, there is a direct exchange interaction between Co and nearby Co atoms, which intends AFM coupling, as shown in Figure 1f. As a result, the ground state is determined by the competition between the superexchange and direct exchange interaction, similar with CrI_3[29] and CGT.[15] In $Co_2Ge_2Te_6$ ML, the superexchange interaction is stronger than the direct exchange interaction. In other words, the superexchange interaction, which originates from the hybridization between Co-d and Te-p orbitals, dominates the exchange interaction, as shown in Figure S3a,b. Finally, $Co_2Ge_2Te_6$ ML intends the FM order.

The geometrical and magnetic properties of $Co_2Ge_2Te_6$ are investigated in the above section, and electronic properties are usually related with the geometry. The band structure and partial density of the states (PDOS) of $Co_2Ge_2Te_6$ are calculated, as shown in Figure 1h,i. The spin-α electron channel is conductive, while the spin-β electron channel is insulative. Therefore, the $Co_2Ge_2Te_6$ is HM, while CGT is a semiconductor with a gap of 0.37 eV, which origins from different d electrons' configuration. The Fermi-level is partially occupied by the spin-α electrons. However, the valance band maximum locates at the Γ point, while the conductance band minimum locates at the K point, for the spin-β electrons. Therefore, $Co_2Ge_2Te_6$ is a semiconductor with an indirect gap of 1.311 eV for spin-β electrons, as shown in Figure 1h. As a result, 100% spin-polarization implies $Co_2Ge_2Te_6$ could be used as spin injection and spin transport devices.[55] Furthermore, the states near the Fermi-level are mainly contributed by Te's p orbitals, while these states are partially contributed by Co's d_{xy}, d_{yz}, $d_{x^2-y^2}$, and d_{xz} orbitals, as shown in Figures 1b, S2a, and S3a, respectively. The PDOS and integrated density of the states (IDOS) of Co atoms are shown in Figure S2a,b, respectively.

3.2. Magnetic and Electronic Properties. Magnetic and electronic properties of $Co_2Ge_2Te_6$ are still unknown, which are worth further research. The different magnetic configurations are investigated to ascertain the magnetic order, shown in Figure 2a−d. Each Co atom contributes 4.0 μ_B MM, and there are eight Co atoms in the 2 × 2 × 1 cell. As a result, there is 32.0 μ_B MM for the FM order. Moreover, three different AFM orders are considered, including AFM-zigzag (AFM-Z), AFM-stripy (AFM-S), and AFM-Néel (AFM-N) orders. For AFM orders, four Co atoms contribute 8.0 μ_B MM, while the other four Co atoms contribute −8.0 μ_B MM. However, MM shows different distributions for different AFM orders. As a result, the total MM equals to 0.0 μ_B, and the corresponding spin charge density difference is shown in Figure 2a−d, respectively. The energy difference is defined as difference between AFM and FM orders. The highest energy of AFM-Z order is 0.69 eV higher than FM order, while the

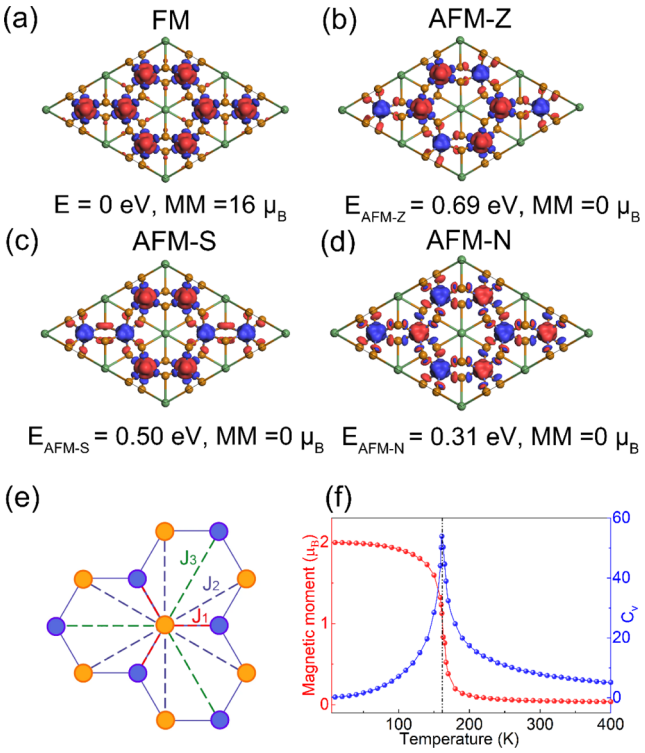


Figure 2. Spin charge density difference of $Co_2Ge_2Te_6$ with (a) FM, and (b) AFM-Z, (c) AFM-S, and (d) AFM-N orders. The red and blue represent spin-α and spin-β electrons. (e) Crystal structure consists of magnetic ion Co only. Illustration of neighbor exchange interactions. J_1, J_2, and J_3 represent the first, second, and third in-plane nearest-neighbor spin−spin exchange interactions, respectively. (f) MM per unit cell (red) and specific heat (C_v) (blue) vary respect to the temperature from Heisenberg model MC simulation, respectively.

AFM-S order has the second highest energy of 0.50 eV, shown in Figure 2b,c, respectively. Moreover, AFM-N order is 0.31 eV higher than the FM order, which has the lowest energy in AFM orders, shown in Figure 2d.

T_c is a significant parameter for ferromagnetic material, and T_c is calculated using the classic Heisenberg model Monte Carlo (MC) with the following formulas

$$H = -J \sum_{<i,j>} S_i \cdot S_j \quad (1)$$

$$E_{FM} = E_0 - (3J_1 + 6J_2 + 3J_3)|S|^2 \quad (2)$$

$$E_{AFM-Néel} = E_0 - (-3J_1 + 6J_2 - 3J_3)|S|^2 \quad (3)$$

$$E_{AFM-zigzag} = E_0 - (J_1 - 2J_2 - 3J_3)|S|^2 \quad (4)$$

$$E_{AFM-stripy} = E_0 - (-J_1 - 2J_2 + 3J_3)|S|^2 \quad (5)$$

where E_{FM}, $E_{AFM-Néel}$, $E_{AFM-zigzag}$, and $E_{AFM-stripy}$ represent energies with FM, AFM-N, AFM-Z, and AFM-S orders, respectively. J and H are the exchange parameter and Hamilton, respectively. Moreover, S_i represents the spin operator, as shown in Figure 2e. The corresponding J_1, J_2, and J_3 represent the nearest-, the next nearest-, and the next−next nearest-exchange parameters. The corresponding J_1, J_2, and J_3 are 3.7, 13.8, and 9.0 meV,[15] respectively. J_2 is large than J_1, and a similar phenomenon also appears in CrB_6-I,[56] and Sr_2FeOsO_6.[57] It could be concluded that long-range magnetic

https://doi.org/10.1021/acs.jpcc.2c08648
J. Phys. Chem. C 2023, 127, 5991−6001

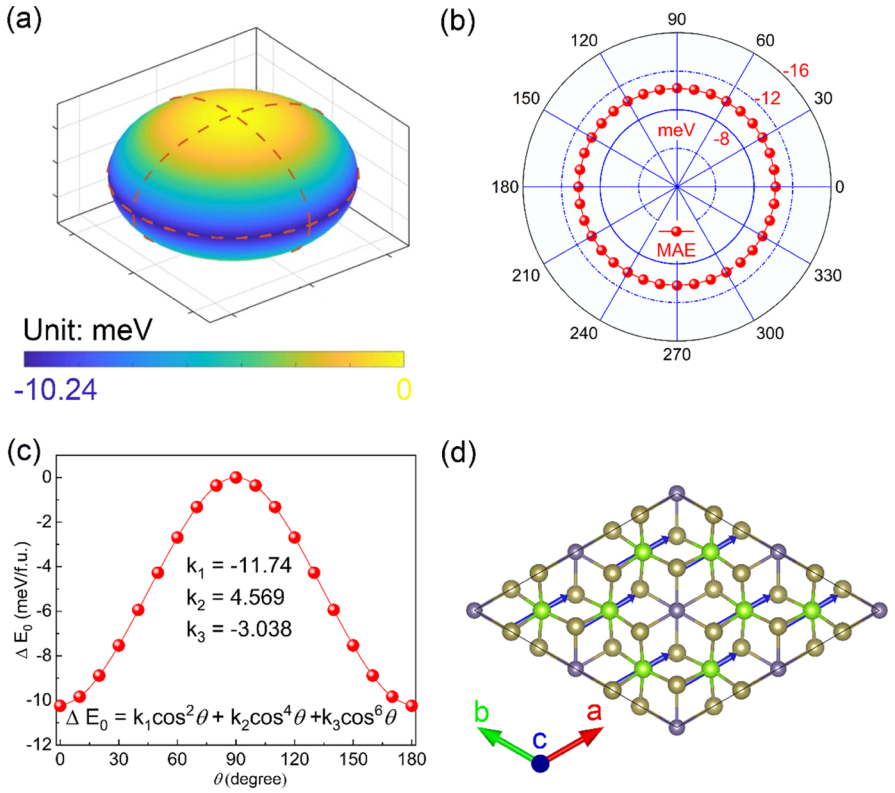


Figure 3. MAE map (FM state as a reference with EA along [001]) of $Co_2Ge_2Te_6$ ML. (a) ΔE_0 varies from the out-of-plane to the in-plane direction. (b) Energy indicated by the dashed lines changes with azimuthal angle φ. (c) ΔE_0 changes with polar angle θ. (d) Blue arrow represents the direction of EA (along [100] direction) of $Co_2Ge_2Te_6$ ML.

interaction also plays a vital role in $Co_2Ge_2Te_6$ ML. Both nearest- and next nearest-neighbor Co atoms show FM couplings. However, J_1, J_2, and J_3 of CGT are 2.71, −0.058, and 0.115 meV, respectively. The corresponding MC code is developed by Prof. Hongjun Xiang's group.[58] As a benchmark, T_c of CrI_3 is calculated to be 51 K,[29] which agrees well with the experiments. A larger 80 × 80 cell with 1.0×10^8 loops is used to evaluate T_c. The 2.0 μ_B MM per Co atom drops quickly. The corresponding T_c is predicted to be 161 K, which is higher than that of CGT (bulk, 66 K).[15]

The electronic properties of materials are usually related with magnetic orders. The FM order is HM, while AFM orders are spin-unpolarized metal or semiconductor, as shown in Figure S4a−d. $Co_2Ge_2Te_6$ ML under different AFM orders are spin-unpolarized semiconductor (AFM-Z order) or metal (AFM-S and AFM-N orders). Therefore, they are different from each other. More discussion could be found in Figure S4 in the Supporting Information.

Co is a heavier element, so the effect of SOC on the electronic properties should be considered. Therefore, the band structures with SOC are also calculated with the HSE06 functional, shown in Figure S5. The band structures with EA along [100] and [001] directions are calculated. There is a Dirac cone above Fermi-level at the K point, when EA is along [100]. However, the Dirac cone appears at the Γ point, as EA is along the [001] direction. Moreover, SOC could cause band splitting in the band structures. Moreover, more detail could be found in Figure S5. Therefore, the band structures with EA along different directions are different from each other.

3.3. Magnetic Anisotropy Properties. MAE means electrons need energy to switch from EA (soft axis) to other direction (hard axis). Therefore, MAE is often used to describe magnetic stability of materials, and an ideal magnetic material is expected to have a larger MAE. In this part, the MAE and MCA energy are calculated using the LDA + U method. The expected magnetic materials in the spintronics are expected to have higher MCA, which means the electron needs more energy to overcome a higher "barrier" from EA to the hard axis. MCA is important for preserving the original direction of magnetic moment from heat fluctuation for the ferromagnetic materials. As $Co_2Ge_2Te_6$ has a D_{3d} point group, the corresponding energy (E) along certain direction (θ, ϕ) follows equations[59]

$$\Delta E_0 = K_1 \cos^2\theta + K_2\cos^4\theta + + K_3 \cos^6\theta + K_4\cos^3\phi \quad (6)$$

$$\Delta E_0 = E - E_{[001]} \quad (7)$$

where $E_{[001]}$ represents the energy along [001] direction. K_1, K_2, and K_3 stand for the quadratic, quartic, and sextic (six degree) contribution to the MAE, respectively. The energy difference ΔE_0 is independent of the in-plane azimuthal angle ϕ. Therefore, K_3 equals to 0, as shown in Figure 3a,b. The eq 6 is simplified into the following equation[60]

$$\Delta E_0 = K_1\cos^2\theta + K_2\cos^4\theta + K_3\cos^6\theta \quad (8)$$

ΔE_0 changes as a function of polar angle θ, as shown in Figure 3c. Moreover, ΔE_0 follows the equation

$$\Delta E_0(\text{meV}) = -11.74\cos^2\theta + 4.569\cos^4\theta - 3.038\cos^6\theta$$

https://doi.org/10.1021/acs.jpcc.2c08648
J. Phys. Chem. C 2023, 127, 5991−6001

for $Co_2Ge_2Te_6$ ML. The MAE and MCA energy could be calculated using following equations

$$MAE = E_{[100]} - E_{[001]} \quad (9)$$

$$MCA = E_{[100]} - E_{[001]} = MAE/S \quad (10)$$

$E_{[100]}$ represents the energy with a magnetic axis along the [100] direction. S is the area of the supercell, and S could be evaluated with this equation: $S = a^2 \sin 60°$, and a is the lattice parameter of the unit cell. The corresponding MAE and MCA energy of $Co_2Ge_2Te_6$ ML is −10.24 meV and −4.001 erg/cm^2, respectively. The negative MAE implies EA points to the in-plane direction, as shown in Figure 3a,d. Compared with CGT (MAE = 0.5 meV),[61] MCA of $Co_2Ge_2Te_6$ is obviously enhanced, and it shows that the Co atom (58.93) is heavier than the Cr atom (51.996). The corresponding SOC in $Co_2Ge_2Te_6$ is stronger than that in CGT. Moreover, MAE mainly comes from the contribution of SOC, similar with VSeTe.[27]

3.4. Dynamical and Thermal Stability. The dynamical stability of $Co_2Ge_2Te_6$ is confirmed via phonon dispersion curves and phonon DOS, which show no obvious imaginary phonon modes. The highest vibration frequency is 6.968 THz, which is lower than CGT (8.364 THz), shown in Figures 4a and S7. From Figure 4b, we can find that the contribution to the low-frequency part ($0 < \varepsilon < 4$ THz) mainly comes from Te atoms. On the contrary, Ge atoms make much contribution to the high-frequency part ($6 < \varepsilon < 7$ THz), while Co atoms contribute to the middle-frequency part ($4 < \varepsilon < 7$ THz).

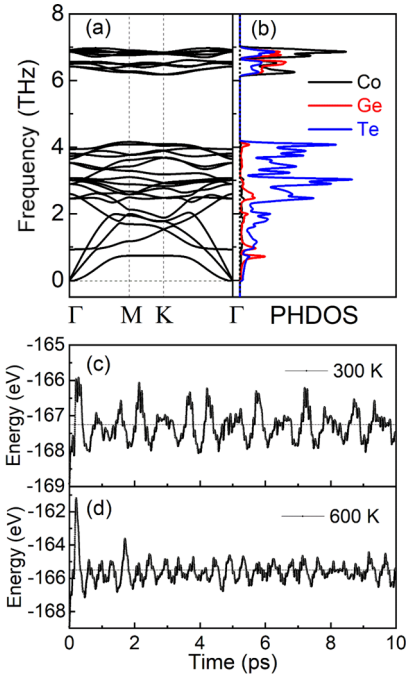


Figure 4. (a) Phonon band structure and (b) density of the states of $Co_2Ge_2Te_6$. The black, red, and blue lines represent partial phonon density of states of Co, Ge, and Te atoms, respectively. (c,d) Total energies change (blue color) with the times at simulated 300 and 600 K, respectively.

The thermal stability of $Co_2Ge_2Te_6$ is evaluated with AIMD. To examine the geometrical stability, we also perform AIMD simulation at 300 and 600 K, respectively. The fluctuation in the total energies is evaluated, and the total energies vibrate around −167.26 eV at 300 K and −165.49 eV at 600 K, as shown in Figure 4c,d, respectively. Moreover, the snapshots of geometries also confirm essential intact structures. No obvious structure distortion is found, so $Co_2Ge_2Te_6$ should be stable at 300 and 600 K.

3.5. Bilayer of $Co_2Ge_2Te_6$. For synthesized 2D materials, one layer intends to antiferromagnetically couple with the other layer, such as CrI_3,[62,63] $NiPS_3$,[64,65] and VSe_2,[66] which inhibits wide application. However, the $Co_2Ge_2Te_6$ bilayer shows the FM order, independent of stacking orders. AA, AA-S-1, AA-S-2, AA-S-3, and AB stackings are fabricated, and the corresponding optimized geometries are shown in Figure 5a–e, respectively. The vertical distance between two layers (d_0) is calculated, as shown in Table 1. The AB stacking has the smallest d_0 of 2.999 Å, which has the lowest binding energy (E_b) −69.23 meV (−120.73 meV with HSE06). Moreover, AA stacking has the second smallest d_0 of 3.605 Å, with E_b of −48.20 meV (−76.79 meV with HSE06). For other stacking orders, such as AA-S-1, AA-S-2, and AA-S-3, d_0 values are 3.742, 4.018, and 4.100 Å, and the corresponding E_b values are −61.57 (HSE06, −96.52), −54.78 (HSE06, −91.52), and −52.18 (HSE06, −84.82) meV, respectively. Therefore, AB stacking is the most stable configuration. Moreover, the ΔE is also related with stacking orders. AA-stacking has the lowest ΔE of −50.0 meV (−63.0 meV with HSE06), while AB-stacking has the second lowest ΔE of −38 meV (−56 meV by HSE06). Other geometries with AA-stackings-(1, 2, 3) also have different ΔE. However, $Co_2Ge_2Te_6$ with different stacking

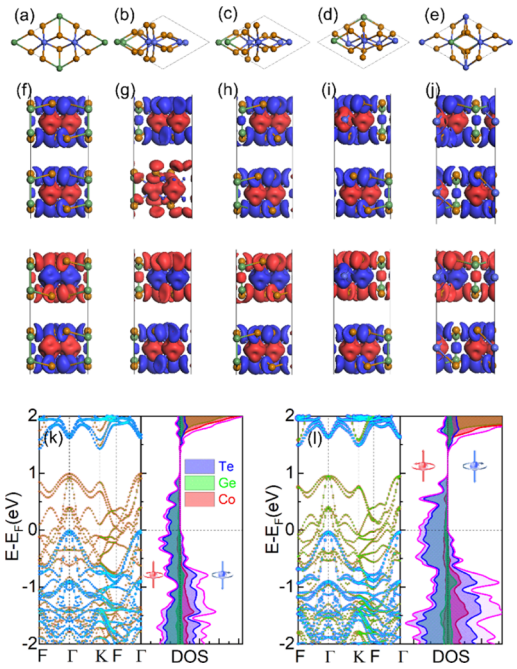


Figure 5. (a–e) Top views of optimized of $Co_2Ge_2Te_6$ with different stacking orders. The top views with stackings of (a) AA, (b) AA-S-1, (c) AA-S-2, (d) AA-S-3, and (e) AB. (f–j) Spin charge density difference of bilayers with different stacking orders. The red and blue represent spin-α and spin-β electrons, respectively. The isovalue is set 0.03 e/Å^3. (k,l) Spin-polarized band structure and PDOS of bilayer with AA and AB stackings, respectively. The red, blue, yellow, pink, cyan, and green represent Te-α, Te-β, Ge-α, Ge-β, Co-α, and Co-β electrons projected band structure, respectively. The red, green, and blue represent Co, Ge, and Te atoms projected PDOS, respectively.

https://doi.org/10.1021/acs.jpcc.2c08648
J. Phys. Chem. C 2023, 127, 5991−6001

Table 1. Distance (d_0) between Two Layers, Binding Energy (E_b), Energy Difference between Different Orders (ΔE), and Electronic Properties with Different Stackings are Calculated by DFT + U and HSE06 Functional, Respectively

	DFT + U			HSE06		propties
system	d_0 (Å)	E_b (meV)	ΔE (meV)	ΔE (meV)	E_b (meV)	HM
AA	3.605	−48.20	−50	−63	−76.79	HM
AB	2.999	−69.23	−38	−56	−120.73	HM
AA-0.993 Å	3.742	−61.57	−11	−27	−96.52	HM
AA-1.324 Å	4.018	−54.78	−31	−51	−91.91	HM
AA-6.083 Å	4.100	−52.18	−19	−34	−84.82	HM

patterns still shows the FM order, which is different from CrI_3.[67] The FM coupling between the interlayers comes from the super−super exchange and vdW interaction between Co atoms in different layers. Moreover, a similar phenomenon also appears in CrI_3 stacking.[67]

The spin charge difference of AA, AA-S-1, AA-S-2, AA-S-3, and AB stackings with FM and AFM orders are shown in Figure 5f,g, respectively. FM order for the bilayers and multilayers is defined as follows: the intralayer Co atoms ferromagnetically couple with each other, and interlayer Co atoms ferromagnetically couple with each other. The AFM order is defined as follows: the intralayer Co atoms still ferromagnetically couple with Co atoms, while the interlayer Co atoms antiferromagnetically couple with each other, as shown in Figure 5f,g. It could be found that MMs mainly localize at Co atoms, while Te and Ge atoms contribute a small part, which is similar with $Co_2Ge_2Te_6$ ML. The most stable configuration is AB-stacking, and each Co atom has 2.43 μ_B MM in the FM order, shown in Figure 5j. However, Co atoms in one layer have 4.86 (2.43 × 2) μ_B MM, while Co atoms in another layer contribute −4.86 (−2.43 × 2) μ_B MM for AFM order, shown in the middle inset of Figure 5j. Co atoms in the AA-stacking contribute 4.87 μ_B MM, while Co atoms in another layer contribute −4.87 μ_B MM for the AFM order, shown in Figure 5f. AA-S-1 (2, 3) stackings show similar phenomena, and the corresponding spin charge differences are shown in Figure 5g−i. The charge difference for AA and AB stackings is also calculated, as shown in Figure S6. It could be found that the charge of accumulation mainly localizes in the interfaces between two layers, as Te atoms get charges, as shown in Figure S6a,b. The depletion area mainly localizes at the vacuum area between two layers.

The electronic properties are usually dependent on the magnetic orders. All the considering stacking orders show FM order, and they are all HMs, as shown in Table 1. The layer projected band structures of AA and AB stackings are calculated with the HSE06 functional, shown in Figures 5k,l and S5a−c, respectively. The $Co_2Ge_2Te_6$ bilayers with AA and AB stackings show HM, and corresponding gaps of spin-β electron are 1.528 and 1.436 eV, respectively, which are larger than ML (1.311 eV). The first and second layers' atoms projected band structures are different from the MoSSe bilayer, which is caused by the quantum confinement. For MoSSe, the conduction and valance bands come from the upper and bottom layers, respectively.[51] However, the upper and bottom layers of $Co_2Ge_2Te_6$ show the same projected band structures, presented in Figure 5k,l. The states near the Fermi-level are mainly contributed by Te atoms, shown in the right columns of the Figure 5k,l, which is the same with ML, as shown in Figure 1i.

3.6. Multilayers of $Co_2Ge_2Te_6$. As the number of layers (N) goes on increasing, the geometry and magnetoelectric properties also change. For N = 3, the ΔE is 0.35 eV (0.058 eV/Co), which implies that 3L $Co_2Ge_2Te_6$ has the $Ferrim_{FM\text{-}FM\text{-}AFM}$ state. $Ferrim_{FM\text{-}FM\text{-}AFM}$ means intralayer Co atoms ferromagnetically couple with other Co atoms, while two interlayer Co atoms antiferromagnetically couple with each other Co atoms. Also, the corresponding spin density is shown in the left inset of Figure 6a. The corresponding PDOS

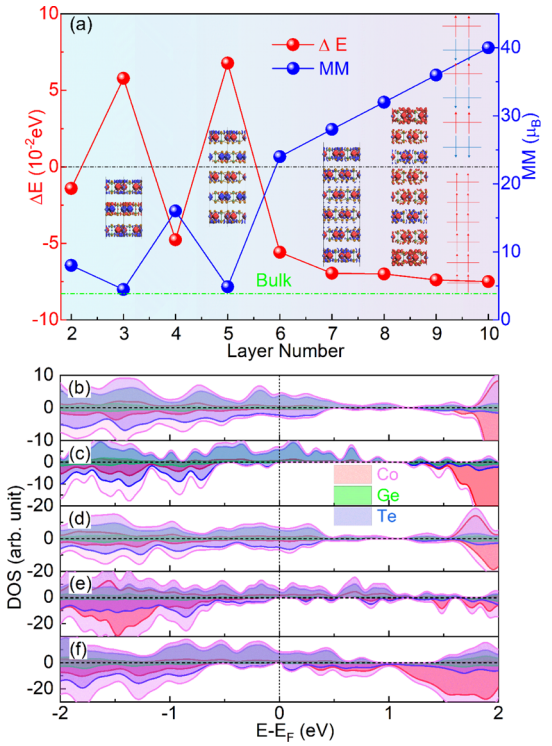


Figure 6. Energy difference and MM change with the layers' numbers. The inset shows the spin densities of 3L, 5L, 6L, and 8L $Co_2Ge_2Te_6$ with ground states. The PDOS of (b) 3L, (c) 4L, (d) 5L, (e) 6L, and (f) 9L with the ground state. The red, green, and blue represent Co, Ge, and Te atoms' PDOS, respectively.

of 3L $Co_2Ge_2Te_6$ is shown in Figure 6b, which implies that 3L is a common spin-polarized metal. Moreover, the states at Fermi-level mainly come from Te atoms' contribution. For N = 4, the ΔE equals to −0.38 eV (−0.048 eV/Co), which means 4L $Co_2Ge_2Te_6$ FM state (inset of Figure 6a), and the corresponding PDOS is shown in Figure 6c, which is similar with 2L $Co_2Ge_2Te_6$ with AB stacking. 4L $Co_2Ge_2Te_6$ with AB stacking is HM. The gap of spin-β electron is 1.216 eV, while spin-α electron is conductive. When the layer of $Co_2Ge_2Te_6$ is increased to five, the spin density is shown in the inset of Figure 6a, and the corresponding PDOS is shown in Figure 6d. It could be concluded that 5L $Co_2Ge_2Te_6$ is a normal spin-

https://doi.org/10.1021/acs.jpcc.2c08648
J. Phys. Chem. C 2023, 127, 5991−6001

polarized metal. As the film becomes thicker, the corresponding ΔE values are −0.06 (N = 6), −0.06 (N = 7), and −0.06 (N = 8) eV, respectively. When N is increased to 9, 10, the corresponding ΔE are increased to −0.07 and −0.08 eV/Co, respectively, which implies multilayers ($N \geq 6$) to be in the FM ground state. It can be concluded that ΔE is close to the bulk (−0.083 eV/Co, shown in Figure 6a), as the $Co_2Ge_2Te_6$ film becomes much thicker. The corresponding PDOS is shown in Figure 6e,f, respectively. They are all HMs, and the similar trend also appears in $CrSe_2$ multilayers.[36] As the thickness increases, the corresponding spin-β electrons' gaps are also decreased to 1.32, 0.97, 0.66, 0.32, and 0.11 eV for N = 6−10, respectively.

It could be concluded that the states near the Fermi-level are also enhanced, as $Co_2Ge_2Te_6$ multilayers become thicker, as shown in Figure 6b−f.

3.7. Bulk of $Co_2Ge_2Te_6$. When the thickness is further increased, the $Co_2Ge_2Te_6$ intends to form bulk. According to the stacking orders of the bilayer, there should be two different stacking orders: bulk-AA and bulk-AB. The corresponding geometry, magnetic, and electronic properties are shown in Figures 7a−h and 8a−g, respectively. Both bulk-AA and AB stackings have a D_{3d} point group, and the corresponding lattice parameters are 7.191 (Figure 7a) and 6.991 (Figure 8a) Å, respectively. The vertical distance between Te atoms is 2.76 Å,

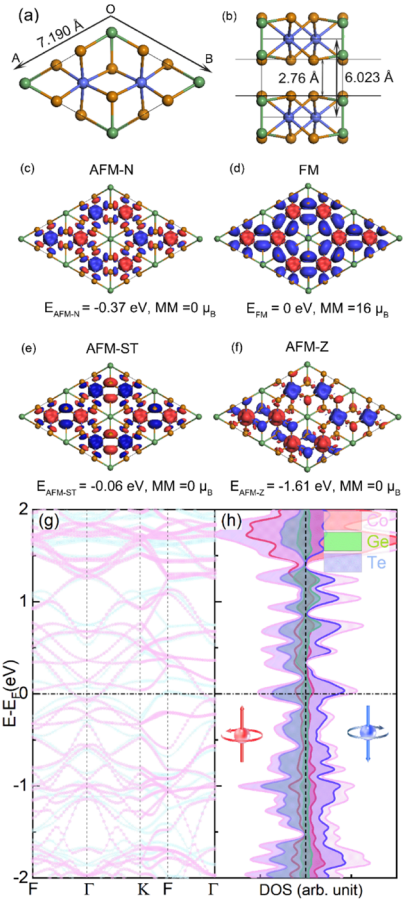


Figure 7. (a) Top and (b) side (along y axis) views of optimized geometries of bulk-AA of $Co_2Ge_2Te_6$. (d,e) Spin charge densities difference of (c) AFM-N, (d) FM, (e) AFM-ST, and (f) AFM-Z orders of ML, respectively. The isovalue is 0.026 e/Å^3. (g) Atom projected band structures. (h) PDOS with FM order. The red, green, and blue lines represent PDOS of Co, Ge, and Te electrons, respectively. The Fermi-level is set to 0 eV.

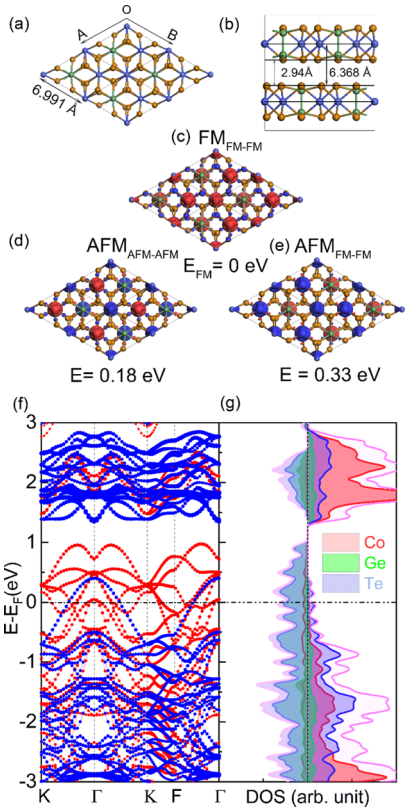


Figure 8. Optimized geometry of $Co_2Ge_2Te_6$ bulk-AB stacking with (a) top and (b) side views. The spin densities of (c) FM_{FM-FM}, (d) $AFM_{AFM-AFM}$, and (e) AFM_{FM-FM} orders, and the isovalue is set to 0.026 e/Å^3. (f) Spin-polarized band and (g) PDOS of the bulk-AB with the FM_{FM-FM} order. The red and blue represent spin-α and spin-β electrons, respectively.

shown in Figure 8b, which is smaller than ML. The bulk-AA shows AFM-Z order, while bulk-AB has FM order, shown in Figures 7 and 8, respectively. For AA stacking, the intralayer Co atoms intend to antiferromagnetically couple Co atoms in the same layer, shown in the right inset of Figures 7a and S8. Moreover, MMs mainly localize in the Co atoms, as shown in Figures 7c−f and S8a,b, similar to ML (Figure 1d,e). The AFM order has a lower energy of −0.33 eV than the FM order for the 1 × 1 × 1 cell. In order to establish magnetic ground state, the AFM-N, FM, AFM-ST, and AFM-Z orders are considered, as shown in Figure 7c−f, respectively. Moreover, the FM order has the highest energy, with the largest MM of 16 μ_B, while the AFM-N order has an energy of −0.37 eV (FM order is taken as reference), as shown in Figure 7c. The AFM-Z order has the lowest energy of −1.61 eV, as shown in Figure 7f. Moreover, the corresponding spin-polarized band structure and PDOS are shown in Figure 7g,h, respectively. The bulk-AA with AFM-Z order is spin-polarized metal, shown in Figure 7g. However, the $Co_2Ge_2Te_6$ ML with the AFM-Z order is a spin-unpolarized semiconductor, shown in Figure S4b. It should be caused by the enhanced interaction between two layers in bulk, as the vertical distance between Co atoms is obviously decreased, as shown in Figure 8b. The states at the Fermi-level are mainly contributed by Te atoms, as shown in Figure 8g, which is similar to ML. Compared with bulk-AA, bulk-AB has

https://doi.org/10.1021/acs.jpcc.2c08648
J. Phys. Chem. C 2023, 127, 5991−6001

Table 2. Matrix Differences for d Orbitals between Magnetization Along [001] and [100] Directions in eqs 12 and 13

	o$^+$					o$^-$				
u$^-$	d_{xy}	d_{yz}	d_{z^2}	d_{xz}	$d_{x^2-y^2}$	d_{xy}	d_{yz}	d_{z^2}	d_{xz}	$d_{x^2-y^2}$
d_{xy}	0	0	0	1	−4	0	0	0	−1	4
d_{yz}	0	0	3	−1	1	0	0	−3	1	−1
$\mathbf{d_{z^2}}$	0	3	0	0	0	0	−3	0	0	0
d_{xz}	1	−1	0	0	0	−1	1	0	0	0
$\mathbf{d_{x^2-y^2}}$	−4	1	0	0	0	4	−1	0	0	0

lower energy. Therefore, bulk-AB (Figure 8a) is more stable. Moreover, the vertical distance of Te atoms of bulk-AB stacking is 2.940 Å, as shown in Figure 8b. The FM order has lower energy than AFM orders in the 1 × 1 × 1 cell. All magnetic orders including these magnetic configurations: FM_{FM-FM}, $AFM_{AFM-AFM}$, and AFM_{FM-FM} orders, are shown in Figure 8a−c, respectively. The subscript FM−FM represents intralayer Co atoms ferromagnetically couple with each other, as shown in Figure 8c. The interlayer Co atoms ferromagnetically couple with each other, which is defined as the FM_{FM-FM} order. The $AFM_{AFM-AFM}$ (Figure 8d) and AFM_{FM-FM} (Figure 8e) orders have higher energies of 0.18 and 0.33 eV than the FM_{FM-FM} order (Figure 8c), respectively. For the FM_{FM-FM} order, Co atoms have 2.37 (1st L), 2.37 (2nd L), 2.42 (2nd L), and 2.42 (1st L) μ_B, respectively, as shown in Figure 8c. For the AFM_{FM-FM} order, Co atoms have 2.35 (1st L), 2.45 (1st L), −2.35 (2nd L), and −2.45 (2nd L) μ_B, respectively, as shown in Figure 8d. However, Co atoms have 2.36 (1st L), −2.42 (1st L), −2.36 (2nd L), and 2.42 (2nd L) μ_B, respectively, as shown in Figure 8e. Compared with the HM of ML, the original states fully occupied by the spin-β electrons are shifted upward as the interlayer interaction enhances. As a result, the fully occupied states are transformed into partially occupied states, which originates from Te's contribution, as shown in Figure 8g. Therefore, bulk-AB is spin-polarized metal, as shown in Figure 8f,g, which should be caused by the enhanced interaction between the interlayer Co atoms. In conclusion, the magnetoelectronic properties are related with stacking orders, and bulk-AA shows a metal with the AFM state, while bulk-AB shows HM with the FM state, respectively.

3.8. Magnetocrystalline Anisotropy. In order to clarify atomic orbital contribution to the MAE, the tight-binding and second-order perturbation theory are adopted in calculating MAE. According to the canonical formulation,[68] MAE of each atom could be evaluated using this equation

$$\mathrm{MAE}_i = \left[\int E_f(E - E_F)[n_i^{[100]}(E) - n_i^{[001]}(E)]\right] \quad (11)$$

where MAE_i represents the MAE of ith atom. $n_i^{[100]}(E)$ and $n_i^{[001]}(E)$ are the DOS of the ith atom with EA along [100] and [001] directions, respectively. $Co_2Ge_2Te_6$ ML has a D_{3d} group. Therefore, the energies with EA along [100] and [010] directions are the same.[25,69] Thus, only the [100] direction is considered here. Moreover, total MAE could be rewritten as the sum of MAE_i: $\mathrm{MAE}_{tot} = \sum_i \mathrm{MAE}_i$. According to the second-order perturbation theory,[70] MAE could be gotten by the sum of the following terms

$$\Delta E^{--} = E_x^{--} - E_z^{--} = \xi^2 \sum_{o^+,u^-} (|\langle o^-|L_z|u^-\rangle|^2 - |\langle o^-|L_x|u^-\rangle|^2)/(E_{u^-} - E_{o^-}) \quad (12)$$

$$\Delta E^{-+} = E_x^{+-} - E_z^{+-} = \xi^2 \sum_{o^+,u^-} (|\langle o^+|L_z|u^-\rangle|^2 - |\langle o^+|L_x|u^-\rangle|^2)/(E_{u^-} - E_{o^-}) \quad (13)$$

where + and − represent spin-α and spin-β states, and ξ, L_x, and L_z are the SOC constant and angular momentum operators along [100] and [001] directions, respectively. u and o represent unoccupied and occupied states, respectively. Moreover, E_o and E_u represent energies of occupied and unoccupied states, respectively.[71] MAE is mainly contributed by spin−orbital matrix elements and energy difference. According to eq 11, MAE is related with the intensity of DOS near the Fermi-level. The matrix element differences $|\langle o^-|L_z|u^-\rangle|^2 - |\langle o^-|L_x|u^-\rangle|^2$ and $|\langle o^+|L_z|u^-\rangle|^2 - |\langle o^+|L_x|u^-\rangle|^2$ for d and p orbitals are calculated, as shown in Tables 2 and 3, respectively. To further interpret MAE changes with number of layers, the atom-orbital-resolved MAE is also analyzed, as shown in Figure 9a−i. It can be found that MAE partially comes from Co (Figure 9a−c) and Ge atoms' contribution (Figure 9d−f), while it mainly comes from Te atoms' contribution (Figure 9g−i). The orbital-resolved MAE of ML is shown in Figure 9a,d,g, respectively. The total MAE is −10.24 meV/f.u., and Te atoms contribute −9.94 meV, shown in Figure 9a,d,g. Moreover, the hybridization between Te's p_y and p_z orbitals contributes −13.33 meV, as shown in Figures 8l and 9g, which corresponds to the matrix differences −1 for p orbital, as shown in Table 3. However, the hybridization between Te atoms' p_x and p_y orbitals, p_x and p_z orbitals contribute 1.76 and 1.63 meV to IMA, which corresponds to the matrix differences 1 for the p orbital, as shown in Figure 9g and Table 3. Compared with Te atoms, Ge's contribution to MAE could be negligible. The hybridization between Co's d_{yz} and d_{z^2}, d_{xy}, and $d_{x^2-y^2}$ orbitals makes negative contribution to MAE (−0.22 and −0.15 meV), which corresponds to the matrix differences −3 and −4 for d orbitals, respectively, as shown in Table 2.

Table 3. Matrix Differences for p Orbitals between EA Along [001] and [100] Directions in eqs 12 and 13

	o$^+$			o$^-$		
u$^-$	p_y	p_z	p_x	p_y	p_z	p_x
p_y	0	1	−1	0	−1	1
p_z	1	0	0	−1	0	0
p_x	−1	0	0	1	0	0

https://doi.org/10.1021/acs.jpcc.2c08648
J. Phys. Chem. C 2023, 127, 5991−6001

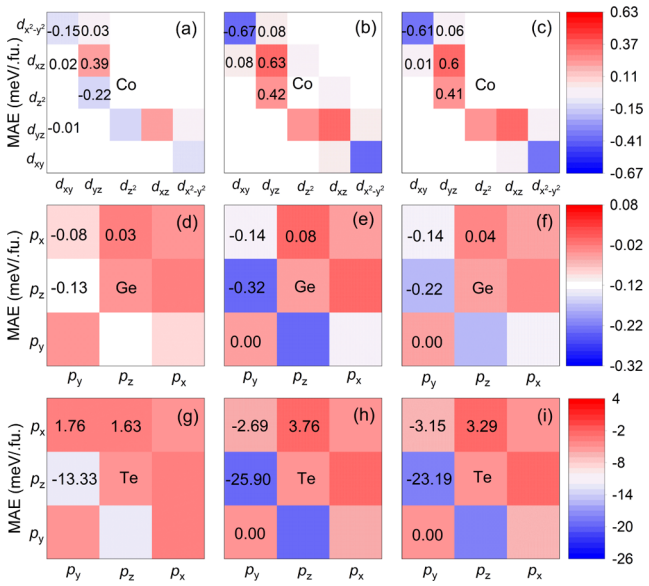


Figure 9. Orbital-resolved MAE of $Co_2Ge_2Te_6$ ML and bilayer with AA and AB stackings, respectively. The orbital-resolved MAE of $Co_2Ge_2Te_6$ (a,d,g) ML, (b,e,h) bilayer with AA, and (c,f,i) AB stackings, respectively.

The hybridization between Co atoms' d_{xz} and d_{yz} orbitals makes positive contribution (0.39 meV) to MAE, which corresponds to the matrix differences +1 for d orbitals.

When two layers are stacked with AA and AB patterns, the orbital-projected MAE is also calculated, as shown in Figures 9b,e,h (AA) and 9c,f,i (AB), respectively. The total MAEs for AA and AB stackings are −24.659 and −24.492 meV, respectively, which are about 2 times of $Co_2Ge_2Te_6$ ML. Te atom contributes −24.83 (AA) and −23.05 meV (AB) to the total MAE, while Co and Ge atoms contribute about 0.54 (AA), −0.38 (AA), 0.47 (AB), and −0.32 meV (AB), respectively. Therefore, the atomic hybridization between Te atomic spin-β occupied p_y and p_z orbitals dominates in-plane magnetic anisotropy (IMA) (−13.33 meV), which corresponds to the matrix differences −1 for p orbitals. However, the hybridization between occupied spin-β p_z orbitals and unoccupied spin-β p_x orbitals makes contribution to perpendicular magnetic anisotropy (PMA) (1.63 meV), which corresponds to the matrix 1 for p orbitals, as shown in Table 3. The atomic hybridization between Te atomic orbitals dominates MAE for AA and AB stackings, which is similar with ML. Moreover, the interactions between p_y and p_z orbitals contribute −25.90 and −23.19 meV for AA and AB stackings, as shown in Figure 9h,i, respectively. In a word, AA and AB have nearly the same MAE, as the two layers show weak vdW interaction. Also, more detail could be found in Figure 9a−h.

4. CONCLUSIONS

In summary, we have predicted and investigated magnetic and electronic properties of $Co_2Ge_2Te_6$ ML with structure search and DFT method. We have found that $Co_2Ge_2Te_6$ ML shows intrinsic ferromagnetism, which comes from the superexchange interaction between Co and Te atoms, and the corresponding bond angle is close to 90°. $Co_2Ge_2Te_6$ is HM with a gap of 1.311 eV for spin-β electrons. The corresponding J_1, J_2, and J_3 of $Co_2Ge_2Te_6$ ML are 3.7, 13.8, and 9.0 meV, respectively. Moreover, $Co_2Ge_2Te_6$ ML has a higher T_c of 161 K. $Co_2Ge_2Te_6$ ML shows IMA, and the corresponding MAE is −10.24 meV/f.u. $Co_2Ge_2Te_6$ shows good dynamical and thermal stability. $Co_2Ge_2Te_6$ bilayer shows robust ferromagnetism and half-metallicity, independent of stacking patterns. All the layers ferromagnetically couple with other layers ($N \geq 6$), while the layer tends to antiferromagnetically couple with other nearby layers for thinner odd layers ($N = 3, 5$). All even and thick odd multilayers are HM, while other multilayers are spin-polarized metal. The magnetoelectronic properties are dependent on the stacking orders for bulk. Bulk-AA shows the AFM order, while bulk-AB shows the FM order. However, they are all normal spin-polarized metal. The super−super exchange interaction and vdW interaction play a key role in the multilayers. Our work represents robust ferromagnetic half-metallic $Co_2Ge_2Te_6$ with high T_c, large MAE, making it a candidate for the new magnetoelectronics.

ASSOCIATED CONTENT

Supporting Information

The Supporting Information is available free of charge at https://pubs.acs.org/doi/10.1021/acs.jpcc.2c08648.

Information on materials, detail of geometry search, K-mesh test, Co-d PDOS and IDOS, Co-d PDOS and Te-p PDOS, band structures with FM and AFM orders, band structures with SOC, charge difference of AA and AB stacking, PDOS of bilayers with different stackings, spin density of bulk with AA, electronic structure of bulk-AA, and calculation of MAE (PDF)

AUTHOR INFORMATION

Corresponding Authors

Zhaoyong Guan − *Key Laboratory of Colloid and Interface Chemistry, Ministry of Education, School of Chemistry and Chemical Engineering, Shandong University, Jinan, Shandong 250100, P. R. China; School of Chemistry and Chemical Engineering, Shandong University, Jinan 250100, P. R. China;* orcid.org/0000-0002-6847-5809; Phone: +86-0531-88363179; Email: zyguan@sdu.edu.cn; Fax: +86-0531-88363179

Shuang Ni − *Research Center of Laser Fusion, China Academy of Engineering Physics, Mianyang, Sichuan 621900, P. R. China*; Phone: +86-0531-88363179; Email: nishuang@163.com; Fax: +86-0531-88363179

Authors

Linhui Lv − *Key Laboratory of Colloid and Interface Chemistry, Ministry of Education, School of Chemistry and Chemical Engineering, Shandong University, Jinan, Shandong 250100, P. R. China*

Ziyuan An − *Key Laboratory of Colloid and Interface Chemistry, Ministry of Education, School of Chemistry and Chemical Engineering, Shandong University, Jinan, Shandong 250100, P. R. China*

Ya Su − *School of Electrical Engineering, Shandong University, Jinan, Shandong 250100, P. R. China*

Yanyan Jiang − *Key Laboratory for Liquid-Solid Structural Evolution & Processing of Materials (Ministry of Education), School of Materials Science and Engineering, Shandong University, Jinan, Shandong 250061, People's Republic of China*

https://doi.org/10.1021/acs.jpcc.2c08648
J. Phys. Chem. C 2023, 127, 5991−6001

Xuming Wu − *College of Physical Science and Technology, Lingnan Normal University, Zhanjiang 524048, P. R. China*

Complete contact information is available at: https://pubs.acs.org/10.1021/acs.jpcc.2c08648

Notes

The authors declare no competing financial interest.

■ ACKNOWLEDGMENTS

We thank Prof. Wenhui Duan, and Xingxing Li for the discussion of evaluation of Curie temperature. We thank Prof. Jun Hu and Jinlong Yang for the discussion of MCA. This work was supported by the financial support from the Natural Science Foundation of China (grant no. 11904203) and the Fundamental Research Funds of Shandong University (grant no. 2019GN065). The authors are grateful to the computational resources from Shanghai Supercomputer Center. The scientific calculations in this paper have been performed on the HPC Cloud Platform of Shandong University. The authors are grateful to Beijing PARATERA Tech Corp., Ltd. for the computation resource in the National Supercomputer Center of Guangzhou. The authors are grateful to Tencent Quantum Laboratory for the computation resource.

■ REFERENCES

(1) Wolf, S. A.; Awschalom, D. D.; Buhrman, R. A.; Daughton, J. M.; von Molnár, S.; Roukes, M. L.; Chtchelkanova, A. Y.; Treger, D. M. Spintronics: A Spin-Based Electronics Vision for the Future. *Science* **2001**, *294*, 1488−1495.

(2) Li, X. X.; Yang, J. L. First-Principles Design of Spintronics Materials. *Nat. Sci. Rev.* **2016**, *3*, 365−381.

(3) Geim, A. K.; Novoselov, K. S. The Rise of Graphene. *Nat Mater* **2007**, *6*, 183−191.

(4) Watanabe, K.; Taniguchi, T.; Kanda, H. Direct-Bandgap Properties and Evidence for Ultraviolet Lasing of Hexagonal Boron Nitride Single Crystal. *Nat Mater* **2004**, *3*, 404−409.

(5) Radisavljevic, B.; Radenovic, A.; Brivio, J.; Giacometti, V.; Kis, A. Single-layer MoS2 transistors. *Nat Nanotechnol* **2011**, *6*, 147−150.

(6) Wang, Q. H.; Kalantar-Zadeh, K.; Kis, A.; Coleman, J. N.; Strano, M. S. Electronics and Optoelectronics of Two-Dimensional Transition Metal Dichalcogenides. *Nat Nanotechnol* **2012**, *7*, 699−712.

(7) Liao, M. H.; Zang, Y. Y.; Guan, Z. Y.; Li, H. W.; Gong, Y.; Zhu, K. J.; Hu, X. P.; Zhang, D.; Xu, Y.; Wang, Y. Y.; He, K.; Ma, X. C.; Zhang, S. C.; Xue, Q. K. Superconductivity in Few-Layer Stanene. *Nat. Phys.* **2018**, *14*, 344.

(8) Wang, B.; Zhou, Q. H.; Wang, J. L. Theoretical Simulation and Design of Two-Dimensional Ferromagnetic Materials. *Chin. Sci. Bull.* **2021**, *66*, 551−562.

(9) Li, D.; Li, S.; Zhong, C.; He, J. Tuning Magnetism at the Two-Dimensional Limit: A Theoretical Perspective. *Nanoscale* **2021**, *13*, 19812−19827.

(10) Mermin, N. D.; Wagner, H. Absence of Ferromagnetism or Antiferromagnetism in One- or Two-Dimensional Isotropic Heisenberg Models. *Phys. Rev. Lett.* **1966**, *17*, 1133−1136.

(11) Huang, B.; Clark, G.; Navarro-Moratalla, E.; Klein, D. R.; Cheng, R.; Seyler, K. L.; Zhong, D.; Schmidgall, E.; McGuire, M. A.; Cobden, D. H.; Yao, W.; Xiao, D.; Jarillo-Herrero, P.; Xu, X. Layer-Dependent Ferromagnetism in a Van Der Waals Crystal Down to the Monolayer Limit. *Nature* **2017**, *546*, 270−273.

(12) Bonilla, M.; Kolekar, S.; Ma, Y.; Diaz, H. C.; Kalappattil, V.; Das, R.; Eggers, T.; Gutierrez, H. R.; Phan, M. H.; Batzill, M. Strong Room-Temperature Ferromagnetism in VSe_2 Monolayers on Van Der Waals Substrates. *Nat Nanotechnol* **2018**, *13*, 289−293.

(13) Fei, Z.; Huang, B.; Malinowski, P.; Wang, W.; Song, T.; Sanchez, J.; Yao, W.; Xiao, D.; Zhu, X.; May, A. F.; Wu, W.; Cobden, D. H.; Chu, J. H.; Xu, X. Two-Dimensional Itinerant Ferromagnetism in Atomically Thin Fe_3GeTe_2. *Nat Mater* **2018**, *17*, 778−782.

(14) Deng, Y.; Yu, Y.; Song, Y.; Zhang, J.; Wang, N. Z.; Sun, Z.; Yi, Y.; Wu, Y. Z.; Wu, S.; Zhu, J.; Wang, J.; Chen, X. H.; Zhang, Y. Gate-Tunable Room-Temperature Ferromagnetism in Two-Dimensional Fe_3GeTe_2. *Nature* **2018**, *563*, 94−99.

(15) Gong, C.; Li, L.; Li, Z.; Ji, H.; Stern, A.; Xia, Y.; Cao, T.; Bao, W.; Wang, C.; Wang, Y.; Qiu, Z. Q.; Cava, R. J.; Louie, S. G.; Xia, J.; Zhang, X. Discovery of Intrinsic Ferromagnetism in Two-Dimensional Van Der Waals Crystals. *Nature* **2017**, *546*, 265−269.

(16) Lohmann, M.; Su, T.; Niu, B.; Hou, Y.; Alghamdi, M.; Aldosary, M.; Xing, W.; Zhong, J.; Jia, S.; Han, W.; Wu, R.; Cui, Y. T.; Shi, J. Probing Magnetism in Insulating $Cr_2Ge_2Te_6$ by Induced Anomalous Hall Effect in Pt. *Nano Lett* **2019**, *19*, 2397−2403.

(17) Hamer, M. J.; Hopkinson, D. G.; Clark, N.; Zhou, M.; Wang, W.; Zou, Y.; Kelly, D. J.; Bointon, T. H.; Haigh, S. J.; Gorbachev, R. V. Atomic Resolution Imaging of $CrBr_3$ Using Adhesion-Enhanced Grids. *Nano Lett* **2020**, *20*, 6582−6589.

(18) Zhao, X.; Song, P.; Wang, C.; Riis-Jensen, A. C.; Fu, W.; Deng, Y.; Wan, D.; Kang, L.; Ning, S.; Dan, J.; Venkatesan, T.; Liu, Z.; Zhou, W.; Thygesen, K. S.; Luo, X.; Pennycook, S. J.; Loh, K. P. Engineering Covalently Bonded 2D Layered Materials by Self-Intercalation. *Nature* **2020**, *581*, 171−177.

(19) Xiong, Y. M. Engineering Two-Dimensional Magnets at Birth. *Nature Electronics* **2022**, *5*, 197−198.

(20) Tang, C.; Zhang, L.; Sanvito, S.; Du, A. Electric-Controlled Half-Metallicity in Magnetic Van Der Waals Heterobilayer. *J. Mater. Chem. C* **2020**, *8*, 7034−7040.

(21) Wei, S. R.; Liao, X. Q.; Wang, C.; Li, J. W.; Zhang, H.; Zeng, Y. J.; Linghu, J. J.; Jin, H.; Wei, Y. D. Emerging Intrinsic Magnetism in Two-Dimensional Materials: Theory and Applications. *2D Mater* **2021**, *8*, 012005.

(22) Butler, S. Z.; Hollen, S. M.; Cao, L.; Cui, Y.; Gupta, J. A.; Gutiérrez, H. R.; Heinz, T. F.; Hong, S. S.; Huang, J.; Ismach, A. F.; Johnston-Halperin, E.; Kuno, M.; Plashnitsa, V. V.; Robinson, R. D.; Ruoff, R. S.; Salahuddin, S.; Shan, J.; Shi, L.; Spencer, M. G.; Terrones, M.; Windl, W.; Goldberger, J. E. Progress, Challenges, and Opportunities in Two-Dimensional Materials Beyond Graphene. *ACS Nano* **2013**, *7*, 2898−2926.

(23) Novoselov, K. S.; Geim, A. K.; Morozov, S. V.; Jiang, D.; Katsnelson, M. I.; Grigorieva, I. V.; Dubonos, S. V.; Firsov, A. A. Two-Dimensional Gas of Massless Dirac Fermions in Graphene. *Nature* **2005**, *438*, 197−200.

(24) Tang, C.; Ostrikov, K.; Sanvito, S.; Du, A. Prediction of Room-Temperature Ferromagnetism and Large Perpendicular Magnetic Anisotropy in a Planar Hypercoordinate FeB_3 Monolayer. *Nanoscale Horiz* **2021**, *6*, 43−48.

(25) Guan, Z.; Ni, S. Prediction of High Curie Temperature, Large Magnetic Crystal Anisotropy, and Carrier Doping-Induced Half-Metallicity in Two-Dimensional Ferromagnetic FeX_3 (X = F, Cl, Br, and I) Monolayers. *J. Phys. Chem. C* **2021**, *125*, 16700−16710.

(26) de Groot, R. A.; Mueller, F. M.; van Engen, P. G.; Buschow, K. H. J. New Class of Materials: Half-Metallic Ferromagnets. *Phys. Rev. Lett.* **1983**, *50*, 2024−2027.

(27) Guan, Z.; Ni, S. Strain-Controllable High Curie Temperature, Large Valley Polarization, and Magnetic Crystal Anisotropy in a 2D Ferromagnetic Janus VSeTe Monolayer. *ACS Appl. Mater. Interfaces* **2020**, *12*, 53067−53075.

(28) Tang, C.; Zhang, L.; Du, A. Tunable Magnetic Anisotropy in 2D Magnets Via Molecular Adsorption. *J. Mater. Chem. C* **2020**, *8*, 14948−14953.

(29) Son, Y. W.; Cohen, M. L.; Louie, S. G. Half-Metallic Graphene Nanoribbons. *Nature* **2006**, *444*, 347−349.

(30) Kan, E. J.; Li, Z.; Yang, J.; Hou, J. G. Half-Metallicity in Edge-Modified Zigzag Graphene Nanoribbons. *J Am Chem Soc* **2008**, *130*, 4224−4225.

(31) Guan, Z.; Si, C.; Hu, S.; Duan, W. First-Principles Study of Line-Defect-Embedded Zigzag Graphene Nanoribbons: Electronic

and Magnetic Properties. *Phys Chem Chem Phys* **2016**, *18*, 12350−12356.
(32) Guan, Z. Y.; Wang, J. J.; Huang, J.; Wu, X. J.; Li, Q. X.; Yang, J. L. Metal-Free Magnetism and Half-Metallicity of Carbon Nitride Nanotubes: A First-Principles Study. *J. Phys. Chem. C* **2014**, *118*, 22491−22498.
(33) Guan, Z. Y.; Wang, W. Y.; Huang, J.; Wu, X. J.; Li, Q. X.; Yang, J. L. Tunable Electronic and Magnetic Properties of Graphene Flake-Doped Boron Nitride Nanotubes. *J. Phys. Chem. C* **2014**, *118*, 28616−28624.
(34) Burch, K. S.; Mandrus, D.; Park, J. G. Magnetism in Two-Dimensional Van Der Waals Materials. *Nature* **2018**, *563*, 47−52.
(35) Hu, X.; Zhao, Y.; Shen, X.; Krasheninnikov, A. V.; Chen, Z.; Sun, L. Enhanced Ferromagnetism and Tunable Magnetism in Fe_3GeTe_2 Monolayer by Strain Engineering. *ACS Appl. Mater. Interfaces* **2020**, *12*, 26367−26373.
(36) Li, B.; Wan, Z.; Wang, C.; Chen, P.; Huang, B.; Cheng, X.; Qian, Q.; Li, J.; Zhang, Z.; Sun, G.; Zhao, B.; Ma, H.; Wu, R.; Wei, Z.; Liu, Y.; Liao, L.; Ye, Y.; Huang, Y.; Xu, X.; Duan, X.; Ji, W.; Duan, X. Van Der Waals Epitaxial Growth of Air-Stable $CrSe_2$ Nanosheets with Thickness-Tunable Magnetic Order. *Nat Mater* **2021**, *20*, 818−825.
(37) Anderson, P. W. Antiferromagnetism. Theory of Superexchange Interaction. *Phy. Rev.* **1950**, *79*, 350−356.
(38) Goodenough, J. B. Theory of the Role of Covalence in the Perovskite-Type Manganites [La, M(II)]MnO_3. *Phy. Rev.* **1955**, *100*, 564−573.
(39) Kanamori, J. Superexchange Interaction and Symmetry Properties of Electron Orbitals. *J. Phys. Chem. Solids* **1959**, *10*, 87−98.
(40) Kresse, G.; Furthmüller, J. Efficiency of Ab-Initio Total Energy Calculations for Metals and Semiconductors Using a Plane-Wave Basis Set. *Comput. Mater. Sci.* **1996**, *6*, 15−50.
(41) Perdew, J. P.; Burke, K.; Ernzerhof, M. Generalized Gradient Approximation Made Simple. *Phys Rev Lett* **1996**, *77*, 3865−3868.
(42) Heyd, J.; Scuseria, G. E.; Ernzerhof, M. Hybrid Functionals Based on a Screened Coulomb Potential. *J. Chem. Phys.* **2003**, *118*, 8207−8215.
(43) Heyd, J.; Scuseria, G. E.; Ernzerhof, M. Erratum: "Hybrid Functionals Based on a Screened Coulomb Potential" [J. Chem. Phys. 118, 8207 (2003)]. *J. Chem. Phys.* **2006**, *124*, 219906.
(44) Liechtenstein, A. I.; Anisimov, V. V.; Zaanen, J. Density-Functional Theory and Strong Interactions: Orbital Ordering in Mott-Hubbard Insulators. *Phys Rev B Condens Matter* **1995**, *52*, R5467−R5470.
(45) Zhang, C. M.; Zhang, L.; Tang, C.; Sanvito, S.; Zhou, B.; Jiang, Z. Y.; Du, A. J. First-Principles Study of a Mn-Doped In_2Se_3 Monolayer: Coexistence of Ferromagnetism and Ferroelectricity with Robust Half-Metallicity and Enhanced Polarization. *Phys. Rev. B* **2020**, *102*, 134416.
(46) Gong, S. J.; Gong, C.; Sun, Y. Y.; Tong, W. Y.; Duan, C. G.; Chu, J. H.; Zhang, X. Electrically Induced 2D Half-Metallic Antiferromagnets and Spin Field Effect Transistors. *Proc Natl Acad Sci U S A* **2018**, *115*, 8511−8516.
(47) Monkhorst, H. J.; Pack, J. D. Special Points for Brillouin-Zone Integrations. *Phys. Rev. B: Solid State* **1976**, *13*, 5188−5192.
(48) Togo, A.; Tanaka, I. First Principles Phonon Calculations in Materials Science. *Scr. Mat.* **2015**, *108*, 1−5.
(49) Nosé, S. A Unified Formulation of the Constant Temperature Molecular Dynamics Methods. *J. Chem. Phys.* **1984**, *81*, 511−519.
(50) Grimme, S. Semiempirical GGA-Type Density Functional Constructed with a Long-Range Dispersion Correction. *J Comput Chem* **2006**, *27*, 1787−1799.
(51) Guan, Z. Y.; Ni, S.; Hu, S. L. Tunable Electronic and Optical Properties of Monolayer and Multilayer Janus MoSSe as a Photocatalyst for Solar Water Splitting: A First-Principles Study. *J. Phys. Chem. C* **2018**, *122*, 6209−6216.
(52) Wang, Y.; Lv, J.; Zhu, L.; Ma, Y. Crystal Structure Prediction Via Particle-Swarm Optimization. *Phys. Rev. B: Condens. Matter Mater. Phys.* **2010**, *82*, 094116.
(53) He, J. J.; Ding, G. Q.; Zhong, C. Y.; Li, S.; Li, D. F.; Zhang, G. Remarkably Enhanced Ferromagnetism in a Super-Exchange Governed $Cr_2Ge_2Te_6$ Monolayer Via Molecular Adsorption. *J. Mater. Chem. C* **2019**, *7*, 5084−5093.
(54) Henkelman, G.; Arnaldsson, A.; Jónsson, H. A Fast and Robust Algorithm for Bader Decomposition of Charge Density. *Comput. Mater. Sci.* **2006**, *36*, 354−360.
(55) Tang, J.; Wang, K. L. Electrical Spin Injection and Transport in Semiconductor Nanowires: Challenges, Progress and Perspectives. *Nanoscale* **2015**, *7*, 4325−4337.
(56) Zhang, Y. L.; Zhang, Y. Y.; Ni, J. Y.; Yang, J. H.; Xiang, H. J.; Gong, X. G. Rational Design of Two-Dimensional Magnetic Chromium Borides Based on First-Principles Calculation. *Chin. Phys. Lett.* **2021**, *38*, 027501.
(57) Kanungo, S.; Yan, B. H.; Jansen, M.; Felser, C. Ab Initio Study of Low-Temperature Magnetic Properties of Double Perovskite Sr_2FeOsO_6. *Phys. Rev. B: Condens. Matter Mater. Phys.* **2014**, *89*, 214414.
(58) Xiang, H. J.; Wei, S. H.; Whangbo, M. H. Origin of the Structural and Magnetic Anomalies of the Layered Compound $SrFeO_2$: A Density Functional Investigation. *Phys Rev Lett* **2008**, *100*, 167207.
(59) Bogdanov, A. N.; Dragunov, I. E. Metastable States, Spin-Reorientation Transitions, and Domain Structures in Planar Hexagonal Antiferromagnets. *Low Temp. Phys.* **1998**, *24*, 852−857.
(60) Kuz'min, M. D.; Richter, M. *Magnetic Anisotropy Calculations: Materials of Technological Interest*; Elsevier: Oxford, 2007; pp 1−7.
(61) Verzhbitskiy, I. A.; Kurebayashi, H.; Cheng, H.; Zhou, J.; Khan, S.; Feng, Y. P.; Eda, G. Controlling the Magnetic Anisotropy in $Cr_2Ge_2Te_6$ by Electrostatic Gating. *Nat. Electron.* **2020**, *3*, 460−465.
(62) Jiang, S.; Xie, H.; Shan, J.; Mak, K. F. Exchange Magneto-striction in Two-Dimensional Antiferromagnets. *Nat Mater* **2020**, *19*, 1295−1299.
(63) Huang, B.; McGuire, M. A.; May, A. F.; Xiao, D.; Jarillo-Herrero, P.; Xu, X. Emergent Phenomena and Proximity Effects in Two-Dimensional Magnets and Heterostructures. *Nat Mater* **2020**, *19*, 1276−1289.
(64) Kang, S.; Kim, K.; Kim, B. H.; Kim, J.; Sim, K. I.; Lee, J. U.; Lee, S.; Park, K.; Yun, S.; Kim, T.; Nag, A.; Walters, A.; Garcia-Fernandez, M.; Li, J.; Chapon, L.; Zhou, K. J.; Son, Y. W.; Kim, J. H.; Cheong, H.; Park, J. G. Coherent Many-Body Exciton in Van Der Waals Antiferromagnet $NiPS_3$. *Nature* **2020**, *583*, 785−789.
(65) Kim, S. Y.; Kim, T. Y.; Sandilands, L. J.; Sinn, S.; Lee, M. C.; Son, J.; Lee, S.; Choi, K. Y.; Kim, W.; Park, B. G.; Jeon, C.; Kim, H. D.; Park, C. H.; Park, J. G.; Moon, S. J.; Noh, T. W. Charge-Spin Correlation in Van Der Waals Antiferromagnet $NiPS_3$. *Phys Rev Lett* **2018**, *120*, 136402.
(66) Cenker, J.; Huang, B.; Suri, N.; Thijssen, P.; Miller, A.; Song, T. C.; Taniguchi, T.; Watanabe, K.; McGuire, M. A.; Xiao, D.; Xu, X. D. Direct Observation of Two-Dimensional Magnons in Atomically Thin CrI_3. *Nat. Phys.* **2021**, *17*, 20−25.
(67) Sivadas, N.; Okamoto, S.; Xu, X.; Fennie, C. J.; Xiao, D. Stacking-Dependent Magnetism in Bilayer CrI_3. *Nano Lett* **2018**, *18*, 7658−7664.
(68) Li, D. Z.; Barreteau, C.; Castell, M. R.; Silly, F.; Smogunov, A. Out- Versus in-Plane Magnetic Anisotropy of Free Fe and Co Nanocrystals: Tight-Binding and First-Principles Studies. *Phys. Rev. B: Condens. Matter Mater. Phys.* **2014**, *90*, 205409.
(69) Guan, Z.; Ni, S. Predicted 2D Ferromagnetic Janus VSeTe Monolayer with High Curie Temperature, Large Valley Polarization and Magnetic Crystal Anisotropy. *Nanoscale* **2020**, *12*, 22735−22742.
(70) Wang, D.; Wu, R.; Freeman, A. J. First-Principles Theory of Surface Magnetocrystalline Anisotropy and the Diatomic-Pair Model. *Phys Rev B Condens Matter* **1993**, *47*, 14932−14947.
(71) Si, C.; Zhou, J.; Sun, Z. Half-Metallic Ferromagnetism and Surface Functionalization-Induced Metal−Insulator Transition in Graphene-like Two-Dimensional Cr_2C Crystals. *ACS Appl. Mater. Interfaces* **2015**, *7*, 17510−17515.

https://doi.org/10.1021/acs.jpcc.2c08648
J. Phys. Chem. C 2023, 127, 5991−6001